Neutron Spin-Echo Instrumentation for Magnetic Scattering

Thomas Keller,* Heiko Trepka, Klaus Habicht, and Bernhard Keimer

Neutron spin-echo (NSE) spectroscopy is a powerful tool for the study of magnon lifetimes and magnetic critical dynamics. The unique property of NSE is the energy resolution in the µeV range. The first NSE spectrometers were optimized for quasielastic scattering at small momentum transfers and delivered substantial contributions to the understanding of critical dynamics in ferromagnets and dynamic correlations in spin glasses. The subsequent resonant NSE (NRSE) technique extends the parameter range toward large momentum and energy transfers and permits to measure magnon lifetimes across the Brillouin zone. NRSE also comprises the Larmor diffraction (LD) mode with a resolution for lattice spacings and their variance $\Delta d_{hkl}/d_{hkl}$ of order 10^{-6}. LD proves useful to determine magnetostriction effects, small lattice distortions related to magnetic ordering, mosaic spread in crystals, and the size distribution of antiferromagnetic domains. Both typical experiments and the related technical innovation are reviewed and an outlook on future developments is given.

1. Introduction

Neutron spin-echo (NSE) uses the Larmor precession of neutron spins in magnetic fields along the flight paths of the incident and scattered neutron beams as an internal clock to detect small changes of the neutron energy in the scattering process.[1,2] At first glance, NSE looks unsuitable for the study of magnetic

T. Keller, H. Trepka, B. Keimer
MPI for Solid State Research
Stuttgart, Germany
E-mail: t.keller@fkf.mpg.de

T. Keller, H. Trepka
MPG Outstation at the MLZ
Garching, Germany

K. Habicht
Department Dynamics and Transport in Quantum Materials
Helmholtz-Zentrum Berlin für Materialien und Energie
Berlin, Germany

K. Habicht
Institut für Physik und Astronomie
Universität Potsdam
Potsdam, Germany

dynamics and spin excitations, as related neutron spin flips disturb the Larmor phase. Hence, it is surprising that seminal experiments at the first NSE spectrometer IN11 designed by Mezei at the ILL were studies of the spin relaxation in spin glasses[3] and on critical magnetic dynamics in ferromagnets.[4] Mezei introduced the instrumental configurations "ferromagnetic NSE" (FNSE) and "intensity-modulated NSE" (IMNSE) for NSE experiments on paramagnetic, ferromagnetic, and spin-depolarizing samples, such as ferromagnets with domains.[5,6]

Since these early experiments at IN11, NSE blossomed into a rich family of spectrometers and techniques.[7] The direct successors of IN11 use long solenoids to generate the precession fields. These IN11-type spectrometers include the IN15 at the ILL[8,9] and the instruments developed by the Jülich Center for Neutron Science at the NIST (Gaithersburg),[10] the SNS (Oak Ridge),[11] and the MLZ (Garching).[12] They are optimized for ultrahigh resolution at small scattering angles to study slow dynamics at large length scales and made significant contributions to the understanding of spin dynamics in spin glasses and magnetically frustrated systems.[13] Multiangle versions of IN11 were designed to gain efficiency by covering large sectors of the scattering angles with detectors. The technical challenge was to generate spacious uniform magnetic precession fields between sample and detectors. The first solution by Farago[14] was the IN11c magnet with ≈30° coverage of scattering angles, a 30 times increase compared with the IN11 single-detector setup, at the cost of a reduced field homogeneity and hence a reduced resolution. The multiangle design was further optimized at the instrument SPAN at HMI (now HZB Berlin). Horizontal Helmholtz coils with opposite current directions generate a radially symmetric horizontal field around the sample. This design allows for a range of scattering angles of nearly 360°.[15] A further innovation for NSE experiments with systems showing complex magnetic order was introduced at SPAN by implementing the cryopad technique at the spin-echo spectrometer.[16,17] With this polarimetric spin-echo technique the matrix elements of the polarization states of the incident and scattered neutron beams are analyzed separately, which is not possible with conventional xyz longitudinal polarization analysis.[2,18] The method enabled the measurement of spin dynamics across the phase diagram of helimagnetic MnSi.[19,20] SPAN was decommissioned with the shutdown of the BER II reactor but found a successor in the instrument WASP at the ILL.[21]

A second class of NSE spectrometers is based on the neutron-resonance spin-echo technique (NRSE) invented by Golub and Gähler,[22,23] where small radio-frequency (RF) spin flippers define the boundaries of the precession regions. These RF flippers contain a static field and an RF field oscillating at resonance with the Larmor frequency of the neutron spin. NRSE offers many degrees of freedom to adapt the design of the RF flippers to specific spectroscopy tasks. Common to all these designs is the stability of the Larmor phase, which is linked to the inherently stable RF. NRSE permits the implementation of inclined precession field boundaries, a prerequisite for the study of dispersive excitations[24] and for Larmor diffraction (LD).[25] NSE instruments designed for measuring lifetimes of excitations in a wide range of momentum and energy transfers are embedded in a three-axis (TAS) background spectometer with a crystal monochromator and analyzer, to preselect a region in momentum and energy transfer (Q, ω). The first instruments of this combined NSE-TAS type were the FLEX-NRSE at HZB,[26,27] TRISP at the MLZ,[28] and ZETA at the ILL.[29] Magnon linewidth data of archetypical antiferromagnets were obtained.[30–32] IN11-type solenoids were implemented in the TASSE project at the TAS spectrometers IN22 at the ILL and PONTA at JAERI (Tokai)[33–35] and gave very good resolution for nondispersive excitations, such as zone-boundary phonons in Ge.[36] A recent development in the field of NSE-TAS uses precession devices (PDs) with static fields (without RF) confined by superconducting Meissner shields to prismatic regions, also referred to as Wollaston prisms.[37,38] First experiments showed a promising performance, both in a measurement of the linewidths and energy renormalization of phonons in Ge[39] and in LD.[40]

The additional degree of freedom to choose different frequencies for the two RF flippers defining the first precession region allows experimenters to generate an intensity-modulated beam with modulation frequencies of several MHz. This is exploited in MIEZE spectrometers.[41] As the intensity modulation is not affected by spin flips from magnetic scattering from spin-depolarizing samples, MIEZE offers the possibility to apply arbitrary fields to the sample, thus facilitating polarization analysis or the use of strong magnets. MIEZE spectrometers are RESEDA at MLZ,[42] at VIN-ROSE at J-PARC,[43] and at the OFFSPEC and LARMOR instruments at ISIS.[44–46] The latter also offer the high-resolution spin-echo small-angle scattering (SESANS) mode,[47,48] which was to date mainly used for nonmagnetic scattering, but could be a powerful technique for the study of magnetic domain morphology. The similar SEMSANS method allows to record the small-angle scattering in parallel with 2D imaging.[49,50]

2. Brief Introduction to NSE

In this section, we review the properties of NSE. 1) The net Larmor phase of a neutron passing through the setup depends to first order only on the energy transfer $\hbar\omega$ in the scattering process and is independent of the variance of the incoming neutron wavevector k_1. This also means that the energy resolution is decoupled from the monochromaticity of the incident beam. 2) The quantity measured in NSE is the polarization P of the

neutron beam at the exit of the precession fields. P is essentially the cosine-Fourier transform in ω of the scattering law $S(\mathbf{Q}, \omega)$, the so-called intermediate scattering function in the time domain $I(\mathbf{Q}, \tau)$. We first consider the case of quasielastic scattering (mean energy transfer of zero) and then the general case of a dispersing excitation. **Figure 1**a shows a generic model of an NSE instrument. Two uniform static (DC) magnetic fields $\mathbf{B}_{1,2}$ of length $L_{1,2}$ along the paths of the incident and scattered neutron beams with wavenumber $\mathbf{k}_{1,2}$ form the PDs. The fields have flat boundaries perpendicular to the beam axis. The incident beam polarization $\mathbf{P}_1$ is perpendicular to $\mathbf{B}_1$. Inside the PD, the neutron spins precess with Larmor frequency $\omega_{L1,2} = \gamma B_{1,2}$, where $\gamma = 2.916\,\text{kHz/Gauss}$ is the "gyromagnetic ratio." The final polarization is given as the average[2]

$$P = \int S(\omega)\cos(\Delta\phi)\,\mathrm{d}\omega \tag{1}$$

where $\hbar\omega$ is the energy transfer and $S(\omega)$ is the energy-dependent part of the scattering law $S(\mathbf{Q}, \omega)$, where we first neglect the $\mathbf{Q}$ dependence. If the field integrals are equal ($\omega_{L1}L_1 = \omega_{L2}L_2$), the net precession angle is

$$\Delta\phi = A/k_1 - A/k_2, \quad \text{with } A = (m/\hbar)\omega_{L1}L_1 \tag{2}$$

m is the neutron mass. The minus sign in Equation 2 results from the antiparallel orientation of $\mathbf{B}_1, \mathbf{B}_2$. With $k_2 = \sqrt{k_1^2 - 2m\omega/\hbar}$ and $k_1 = \overset{\circ}{k}_1 + \Delta k_1$, where $\overset{\circ}{k}_1$ is the mean and Δk_1 is the variance of k_1, the first-order term of Equation (2) is

$$\Delta\phi = \omega\tau_{\text{NSE}}, \quad \text{with } \tau_{\text{NSE}} = \frac{m^2\omega_{L1}L_1}{\hbar^2(\overset{\circ}{k}_1)^3} \tag{3}$$

The constant τ_{NSE} is called "spin-echo time" with values up to 1 µs in modern IN11-type spectrometers, corresponding to an energy resolution of the order of a few neV. The variance Δk_1 would appear in the second-order terms of Equation (3) but is negligible for quasielastic scattering if $\Delta k_1/\overset{\circ}{k}_1 < 0.2$. For the typical Lorentzian $S(\omega) = \Gamma/[\pi(\Gamma^2 + \omega^2)]$ with linewidth Γ (half-width at half-maximum, Equation 1) gives an exponential decay $P(\tau_{\text{NSE}}) = \exp(-\Gamma\tau_{\text{NSE}})$. An intuitive physical interpretation of τ_{NSE} in terms of a longitudinal splitting of wave packets related to the up and down spin states is given in other studies.[51,52]

Now we review the general case of NSE applied to dispersive excitations. Here the measurement principle also relies on the linear relation of phase and energy transfer (Equation (3)), but the second-order terms tend to be much larger than in the case of quasielastic scattering. These terms are related to the instrument configuration and sample properties, including beam collimation and monochromatization, scattering geometry, excitation energy, and slope and curvature of the dispersion branch.[53,54] To keep higher orders small compared with the essential first-order $\omega\tau_{\text{NSE}}$, the variance of $k_{1,2}$ has to be limited using a (crystal) monochromator (M) and analyzer (A), so that the spin-echo PDs are embedded in a three-axis spectrometer (TAS). The instrumental resolution of this so-called "background" TAS is an ellipsoid-shaped function $R(\mathbf{Q}, \omega)$ (**Figure 2**) giving the
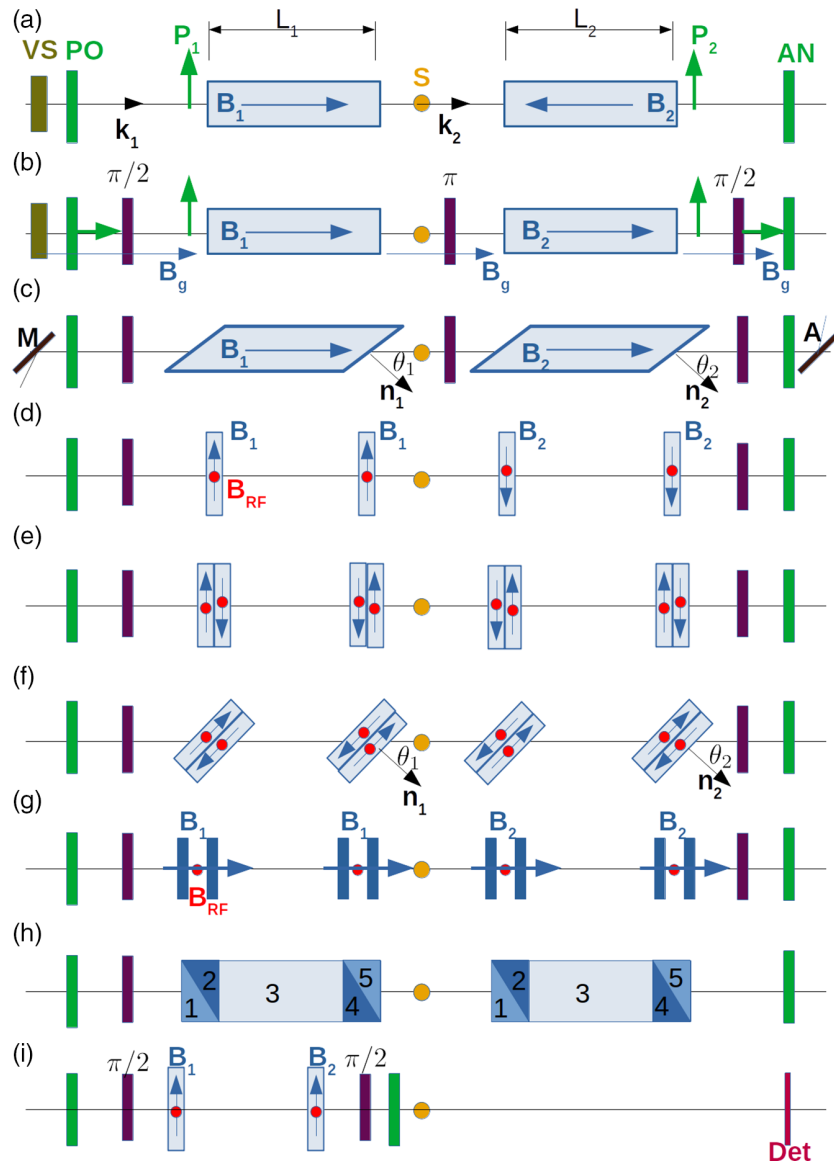
Figure 1. The NSE family. VS: velocity selector; PO: polarizer; AN: polarization analyzer; S: sample; M: monochromator; A: energy analyzer; $\pi/2, \pi$: flippers; $\theta_{1,2}$: inclination angles; $\mathbf{n}_{1,2}$: normal vectors.

probability to detect a scattering event at $(\mathbf{Q}, \omega)$ located on a dispersion sheet around a central value $(\mathbf{Q}_0, \omega_0)$.

The dark blue disks sketched inside the ellipsoid are the planes of constant spin-echo phase, which are tuned by proper choice of the PD parameters to be oriented tangential to the dispersion surface. All scattering events on such a plane will accumulate the same Larmor phase $\Delta\phi$, and the phase of other scattering events inside the region defined by the ellipsoid will vary proportional to $\hbar\omega$, independent of Q. The basic NSE instrument with TAS background spectrometer is shown in Figure 1c, where besides the crystal monochromator (M) and AN (A), the variable inclination angles $\theta_{1,2}$ of the field boundaries are introduced as additional parameters. $\mathbf{n}_{1,2}$ are unit vectors normal to the field boundaries. The instrumental tuning conditions for the

field inclination at the nominal excitation $(\mathbf{Q}_0, \omega_0)$ depend on the slope of the dispersion $\nabla_{\mathbf{q}}\omega_0(\mathbf{q}_0)$.

$$\mathbf{n}_{1,2} = \frac{\mathbf{N}_{1,2}}{N_{1,2}} \text{ with } \mathbf{N}_{1,2} = \frac{\hbar}{m}\mathbf{k}_{1,2}^\circ - \nabla_{\mathbf{q}}\omega_0(\mathbf{q}_0) \text{ and } N_{1,2} = |\mathbf{N}_{1,2}|$$

(4)

and

$$\frac{\omega_{L1}L_1}{\omega_{L2}L_2} = \frac{N_1(\mathbf{k}_1^\circ \cdot \mathbf{n}_1)^2 \cos\theta_2}{N_2(\mathbf{k}_2^\circ \cdot \mathbf{n}_2)^2 \cos\theta_1}$$

(5)

Definitions of $\theta_{1,2}$ are shown in Figure 1c. The spin-echo time is then
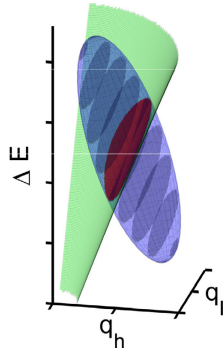
Figure 2. The TAS-resolution ellipsoid (blue) cuts a small section (red) of the curved dispersion surface (green). The planes of constant NSE phase (dark blue) are parallel to a plane oriented tangentially to the dispersion surface.

$$\tau_{NSE} = \frac{m\omega_{1,2} L_{1,2} \cos\theta_{1,2}}{\hbar(k^{\circ}_{1,2} n_{1,2})^2 N_{1,2}} \tag{6}$$

In the preceding equation, the parameters either for the first or the second PD can be used, and both give the same result for τ_{NSE} if the instrument is tuned to Equation (4) and (5). Here we use the definitions $\mathbf{Q}_0 = \mathbf{q}_0 + \mathbf{G}_0 = \mathbf{k}^{\circ}_1 - \mathbf{k}^{\circ}_2$, $\omega_0 = \omega(\mathbf{q}_0) = \hbar/(2m)((\mathbf{k}^{\circ}_1)^2 - (\mathbf{k}^{\circ}_2)^2)$, $\Delta\omega = \omega - \omega_0$. $\mathbf{G}_0$ is a reciprocal lattice vector. The final polarization is

$$P(\tau_{NSE}) = F(\tau_{NSE}) \times \int S(\mathbf{q}_0, \Delta\omega) \cos(\Delta\omega \times \tau_{NSE}) d(\Delta\omega) \tag{7}$$

The factor $F(\tau_{NSE})$ is the spin-echo resolution function that contains the aforementioned second-order terms.[53,54] Equation (7) shows the characteristic property on NSE, that the measured signal is a product of the instrumental resolution and the Fourier transform of $S(\omega)$, whereas in conventional spectrometry, these two terms are convoluted.

3. The NSE Family

In this section, we briefly review the various types of spin-echo spectrometers and their properties. These designs fall into two categories. The first one is focused on maximum resolution for slow quasielastic scattering processes and the second one is optimized for the study of dispersive excitations and LD. Both have proven useful for the study of magnetic scattering. The archetype of the high-resolution instruments is the first NSE spectrometer IN11 at the ILL, designed by Mezei.[1] The backbone of the IN11-type instruments (Figure 1b) is two solenoids, generating longitudinal DC fields ($B_{1,2}$), where in contrast to the simple model in Figure 1a, these fields are aligned parallel, with a small longitudinal guide field B_g extending toward the polarizer (PO) and polarization analyzer (AN) and in the sample region. The reason for the parallel alignment is that antiparallel ($B_{1,2}$) would result in an ill-defined field reversal with a zero transition close to the sample. Such field reversals tend to depolarize the neutron beam. The guide field B_g also defines the quantization axis for the PO and AN, such that the initial beam polarization P is parallel to B_g. Additional

$\pi/2$ flippers rotate P from parallel to perpendicular B_g to start and stop the Larmor precession, and a π flipper close to the sample inverts the Larmor phase acquired in B_1 ($\phi_1 \rightarrow -\phi_1$), which is equivalent to antiparallel $B_{1,2}$.

The second approach is the resonant spin-echo technique,[23] where the PD is formed by a pair of RF flippers bounding the precession region (Figure 1d). These flippers incorporate DC fields $B_{1,2}$ and RF fields $B_{RF1,2}$ oscillating at the Larmor frequency $\omega_{1,2} = \gamma B_{1,2}$. The setup is equivalent to a static field $2B_{1,2}$ of the same length $L_{1,2}$, resulting in an effective Larmor frequency $2\omega_{L1,2}$. A further amplification with an effective Larmor frequency of $4\omega_{L1,2}$ is obtained in the "bootstrap" setup with double RF flippers and antiparallel DC fields (Figure 1e).[22] Besides a higher effective Larmor frequency, the latter has the advantage of very low DC stray fields outside the flippers, such that the whole beam path between the $\pi/2$ flippers can be housed inside a mu-metal magnetic shield to reduce the sensitivity to external fields. Inclined field boundaries are easily achieved by rotating the RF flippers (Figure 1f). Such RF bootstrap flippers with DC fields transverse to the beam axis are used at the TAS spectrometers TRISP, ZETA, and FLEXX (decommissioned). One disadvantage of the transverse field flipper type is that the neutron beam has to transmit the windings of the coils. To minimize absorption, the thickness of the wires has to be minimized, but this also increases resistive heating, such that the DC field and τ_{NSE} are limited to significantly smaller values than those reachable by the IN11-type solenoid design.

A solution to increase the resolution given by the maximum field in NRSE spectrometry is the so-called longitudinal (L)-NRSE technique used at the RESEDA spectrometer (Figure 1g), where large DC fields are generated parallel to the beam axis, either by short solenoids or by Helmholtz coils, such that the beam only transmits the winding of the RF coil.[42,55] The precession field strength obtained by the first-generation L-NRSE is comparable with that of the IN11-type spectrometers, but the latter still can handle much larger beam cross sections. L-NRSE has many degrees of freedom for optimizing the performance, but it is limited to nondispersive excitations, as there is no option to incline the field boundaries.

The RF flippers at the LARMOR and OFFSPEC instruments at ISIS use transverse DC fields generated by iron-yoke electromagnets and RF fields longitudinal to the beam axis, such that the beam transmits the coil freely without touching any wires.[44–46,56] The beam cross section for these coils is limited, but the design is very good for applications in reflectometry[57–59] and SESANS,[47,60,61] where additional SANS in the coils has to be avoided. Wedge-shaped pole pieces on the electromagnets also allow for inclined field boundaries.

A novel PD design is based on superconducting Wollaston prisms with transverse DC fields, as shown in Figure 1h.[37,38,40] All field sections B_{1-5} are tunable without significant crosstalk between them. Although the geometry is fixed, arbitrary effective field inclination angles can be set. Thus, the device is useful for the study of excitations and for LD.[40] The performance of the first prototype devices is already close to the transverse RF flippers, and recently RF coils were incorporated in these superconducting devices to further enhance the effective Larmor frequency and the phase stability.[62]

MIEZE (Figure 1i) is basically a time-of-flight (TOF) method, where fast-intensity modulation of a neutron beam is generated by RF flippers and a subsequent AN. The resulting intensity modulation reaches frequencies in the MHz range, whereas mechanical choppers can at best reach a few kHz. The challenge is the detection of such a fast-intensity modulation, which is smeared out by the variance in Δk_i. Assume for example typical cold neutrons of wavelength $\lambda = 4\,\text{Å}$ and velocity $v = 1000\,\text{m s}^{-1}$ modulated at 1 MHz and a monochromaticity of $\Delta k_i/k_i = 0.05$. After ≈ 20 modulation periods corresponding to a neutron path of 20 mm, the modulation is averaged to zero. A solution to recover the fast-intensity modulation at a focal point corresponding to the location of the neutron detector was first found by Golub and Gähler for a mechanical chopper system, called FOTOF,[63] and later transferred to RF flippers.[41] Figure 1i shows the basic MIEZE configuration. Two RF flippers upstream the sample are operated at different fields $B_{1,2}$ with resonant frequencies $\omega_{L1,2}$, with $\omega_{L2} > \omega_{L1}$. Then, at the exit of RF flipper 2, the polarization is modulated by $\Delta\omega_M = 2(\omega_{L2} - \omega_{L1})$ (the factor 2 applies for single RF flippers), and the modulation recovers at the focal plane at $L_2 = L_1/(\omega_{L2}/\omega_{L1} - 1)$. L_1 and L_2 is the distance between the RF flippers and between the second RF flipper and the detector, respectively. The range of $\Delta\omega_M$ is limited by the coupling to the focal length L_2 via the ratio and difference of $\omega_{L1,2}$. An additional DC field B_f in between the RF flippers allows for independent tuning of L_2 and thus for a wider range of $\Delta\omega_M$.[64] After passing the $\pi/2$ flipper and polarization analyzer (AN), the modulation of the polarization is converted to an intensity modulation $I(t) \sim 1 + C\sin(\Delta\omega_M t)$, with

$$C(\tau_M) = \int S(\omega)\cos(\omega\tau_M)\,d\omega \quad \text{with} \quad \tau_M = \frac{m\Delta\omega_M L_D}{\hbar(k_i^{\circ})^3} \tag{8}$$

The intensity modulation is not affected by spin flips in the sample, such that investigation of ferromagnetic samples[65,66] and application of high magnetic fields[67] is possible. One limitation of MIEZE is the sensitivity to path length variation of the neutron trajectories, which increases with the scattering angle and the sample size.[68,69] Hence, MIEZE is more powerful for small-scattering angles. At larger scattering angles, very good resolution is only achieved if the sample size parallel to Q is small (in the order of 1 mm), whereas the sample dimension perpendicular to Q has little effect on the path length. As the AN is placed upstream of the sample, the beam incident on the sample is polarized, such that both longitudinal polarization analysis and polarimetry can be applied.

LD is a high-resolution technique closely related to spin echo. First, LD is based on Larmor precession in DC fields or RF flippers with inclined field boundaries and is thus readily available on N(R)SE-TAS instruments. Second, LD delivers information necessary to interpret and analyze spectroscopic NSE data, including accurate thermal expansion data, information about structural distortions and magnetostriction related to magnetic ordering, and mosaicity and microstrains related to crystal quality. The characteristic limitation of conventional diffractometers imposed by the inverse proportionality between intensity and resolution is not effective in LD, and excellent momentum resolution without excessive loss of intensity is achieved. In this respect, LD is similar to NSE, where the energy resolution is decoupled from the monochromaticity of the incident neutron beam. The drawing in **Figure 3**a shows the field configuration proposed by Rekveldt,[25,70] which comprises two DC fields $B_{1,2}$ with boundaries parallel to the lattice planes or perpendicular to the reciprocal lattice vector G_{hkl}. Note that there is no π flipper, such that the phases add. The phase is proportional to the transition time $t = mL/(\hbar k_\perp)$ the neutron spends in the field regions. The momentum perpendicular to the field boundary $k_\perp = G_{hkl}/2 = \pi/d_{hkl}$ is selected by the Bragg reflection, so that all neutrons reflected at the lattice planes d_{hkl} acquire the same phase, independent of the Bragg angle.

$$\phi_{LD} = \frac{2m\omega_L}{\hbar\pi}d_{hkl} \tag{9}$$

A variation of d_{hkl}, for example, by thermal expansion, is measured by tracking the phase shift $\Delta\phi(T) = \phi_{LD} \times \epsilon_{hkl}$ versus the temperature T, where
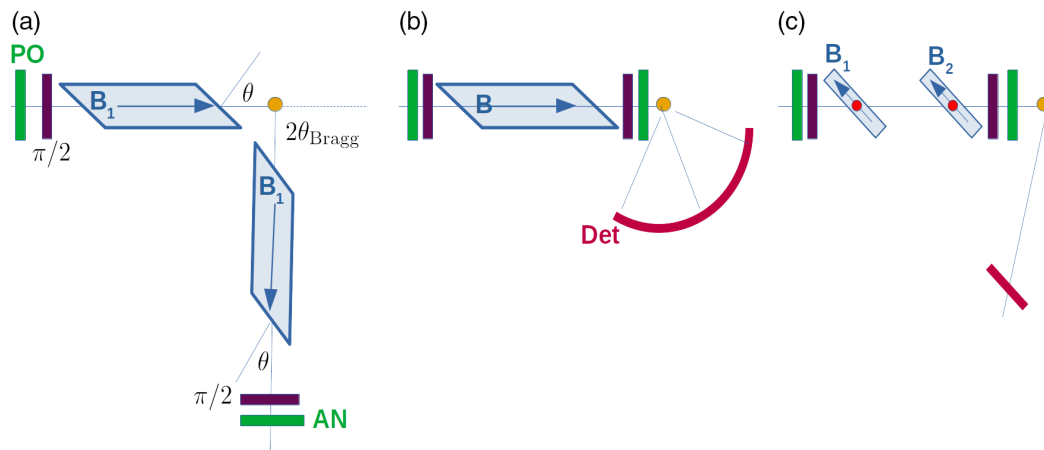

Figure 3. Larmor diffractometer layouts. a) Standard LD. b) Single-arm LD. c) MIEZE LD. PO: polarizer; AN: polarization analyzer; DET: neutron detector; $\pi/2$ flipper.

$$\epsilon_{hkl} = d_{hkl}/d_{hkl}^{\circ} - 1 \qquad (10)$$

d_{hkl}° is the mean or unperturbed value of d_{hkl}. d_{hkl} is typically spread, for example, by the effect of microstrains. Then the phase is also spread as

$$\Delta\phi_{LD} = \phi_{LD}^{\circ} \times \epsilon_{hkl} \qquad (11)$$

ϕ_{LD}° is related to d_{hkl}° via Equation 9. The final beam polarization is given by the average

$$P_{LD}(\phi_{LD}) = \langle\cos(\Delta\phi_{LD})\rangle = \int D(\epsilon_{hkl})\cos(\phi_{LD}\epsilon_{hkl})\mathrm{d}\epsilon_{hkl} \qquad (12)$$

D is the distribution function of ϵ_{hkl}. The benefit of using two PDs is not obvious for LD on single crystals, except for the gain factor 2 in Equation 9, but becomes apparent for mosaic or polycrystalline samples, where the lattice planes deviate from the ideal orientation parallel to the field boundaries. In this case, the Larmor phases in the first and second PD are different, but the sum ϕ_{LD} stays constant, such that the resolution is not limited by the crystal mosaic. For powder samples, the resolution might be degraded by parasitic small-angle scattering of the neutrons inside the sample, but this effect is minimized by proper design of the shape of the sample containers.[71] As LD is difficult to integrate into conventional powder diffractometers with multiangle detectors, Rekveldt suggested the configuration in Figure 3b using only one PD upstream of the sample, at the cost of a reduced resolution.[72,73] Such an instrument could enhance the resolution of powder diffraction by one order of magnitude toward $\epsilon_{hkl} \sim 10^{-5}$, that is about one order of magnitude less than for the standard LD configuration with two PDs. Below we will discuss a combination of LD and MIEZE for the design of future instruments.

4. Spin-Echo View of Magnetic Scattering

In this section, we discuss the spin-flip processes related to magnetic scattering in view of N(R)SE. This discussion is valid for all types of spin-echo spectrometers, but there are also differences. At NSE-type spectrometers with DC precession fields there is a small guide field at the sample, which also defines a quantization axis for the spin, whereas at NRSE-TAS instruments, the sample is typically located in a zero-field region, and the spin projection on a quantization axis given by the guide field occurs at the transition from the zero field to the guide field region of the AN. Here we will use the geometry of the TRISP spectrometer, as the experimental examples shown in the following section were all measured at this spectrometer. In contrast to the usual 1D polarization analysis,[18] where the polarization of the incident neutrons is defined by a guide field at the sample, in NSE, the phases ϕ_1 of the spins of the incident neutrons s_1 are spread by $\Delta\phi_1$ within the xy plane ("precession plane" $\perp B_1$) due to the variance of k_1, where typically $\Delta\phi_1 \gg 2\pi$ (**Figure 4**).

Mezei pointed out that the magnetic fluctuations M_y and M_z parallel and perpendicular to the xy-precession plane have to be distinguished.[3] As the x-axis is defined to be parallel Q, the component M_x does not contribute to the scattering cross section. The spin flips can be considered as a rotation by π on a cone defined by the angle between s_1 and the magnetic fluctuations
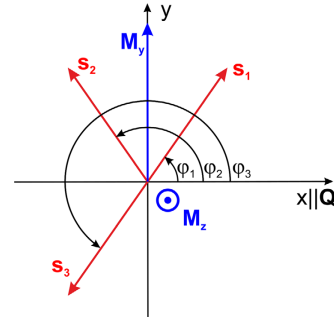

Figure 4. Spin flips and Larmor phase at the sample. The spins of the incident beam are spread within the xy-plane, the precession plane $\perp \mathbf{B}_0$, with $x\|\mathbf{Q}$, z is vertical. The magnetic fluctuations $M_y, M_z \perp \mathbf{Q}$ contribute to the scattering cross section. The spin s_1 with ϕ_1 of an incident neutron is flipped to s_2 or s_3 by M_y or M_z, respectively. The corresponding phases are $\phi_2 = \pi - \phi_1$ and $\phi_3 = \pi + \phi_1$.

M_y or M_z, which flip s_1 to s_2 or s_3, respectively. The related phases are $\phi_2 = \pi - \phi_1$ or $\phi_3 = \pi + \phi_1$. ϕ_2 already includes the sign change of ϕ_1 and thus effectively inverts the direction of the first precession region, whereas ϕ_3 includes only an additional phase π, but no sign inversion of ϕ_1. Thus, to fulfill the echo condition, for the M_z fluctuations, the polarity of the PDs is chosen antiparallel or a π flipper is used as in the case of nonmagnetic scattering, whereas for the M_y fluctuations, the PDs are poled parallel or the π flipper is omitted. If both M_y and M_z are present, the configuration giving the better signal amplitude is chosen experimentally. For large τ_{NSE}, the neutrons scattered by the fluctuations fulfilling the echo condition contribute to the polarized signal, whereas the other fraction generates a nonpolarized background reducing the signal polarization. In this case, Equation 1 applies with a constant prefactor P_0, where $P_0 = 0.5$ for equal population of M_y and M_z. For small τ_{NSE}, spin flips from $\mathbf{M}_{y,z}$ give oscillating signals, which require a numerical analysis beyond the simple Equation (1), as demonstrated in the example on critical scattering below.

In ferromagnetic samples, the neutron spins acquire an additional Larmor phase with a large variance depending on the domain sizes and orientations,[74] such that all spin-echo-related phase information is lost. Farago introduced an IMNSE configuration with additional POs up- and downstream of the sample, which recover 50% of the spin-echo signal[5] at the cost of a 75% intensity reduction. The principle is that across the sample the Larmor phase is converted to an intensity modulation $I(\Delta k_1)$. This IMNSE scheme was also used to combine polarimetric analysis based on cryopad with NSE.[16,17,20] The MIEZE method also is not affected by spin flips, as the Larmor phase is converted to an intensity modulation $I(t)$, in analogy to IMNSE. In addition, either conventional 1D polarization analysis or polarimetry could be combined with MIEZE but limited to dispersionless excitations.

5. Examples from TRISP

Here we show examples focusing on the present potential of NRSE-TAS at the TRISP spectrometer. These include the textbook case of antiferromagnetic (AF) magnons in 3D and

**ADVANCED
SCIENCE NEWS**

www.advancedsciencenews.com

pss b
physica status solidi

www.pss-b.com

quasi-2D spin-5/2 systems MnF_2 and Rb_2MnF_4, respectively, the critical scattering in these compounds for $T \geq T_N$, spin excitation linewidths in a 1D chain material, and examples from LD related to magnetic ordering.

5.1. Magnon Lifetimes and Critical Dynamics in 2D and 3D Antiferromagnets

Rb_2MnF_4 and MnF_2 are textbook examples for 2D and 3D Heisenberg antiferromagnets with a small uniaxial anisotropy resulting from dipolar spin−spin interactions. Previous calculations of the magnon linewidth (inverse lifetime) based on four-magnon scattering and linewidth data from conventional neutron spectroscopy showed considerable disagreement. The discrepancy resulted both from necessary approximations in the analytical calculations and from limited resolution in neutron spectroscopy. In other studies,[30,75] NRSE data with a significantly improved resolution ($\approx 1\,\mu eV$) show excellent agreement with a numerical calculation using the aforementioned four-magnon scattering process including Umklapp processes and domain-wall scattering. Momentum-resolved linewidth data and related accurate calculations provide the basis to calculate the magnon-mediated thermal conductivity without depending on adjustable parameters.[76]

High-resolution NRSE data for the magnon linewidths were collected both for Rb_2MnF_4 and for MnF_2 across the Brillouin zone (BZ), in the AF-ordered state between 3 K and 0.6 T_N (T_N is 38.4 K for Rb_2MnF_4 and 67.6 K for MnF_2). Both systems have a tetragonal structure, and the dominating magnetic interaction is the exchange coupling between the $s = 5/2$ Mn^{2+} spins. The uniaxial AF spin alignment along the crystallographic c-axis is due to an uniaxial anisotropy arising from dipole−dipole interactions. Referring to Figure 4, with alignment of the crystallographic c-axis $\parallel z$, only the M_y fluctuations contribute to the scattering cross section. This implies that the parallel field configuration of the spectrometer, corresponding to NSE without π flipper, gives the echo condition. Raw spin-echo data from MnF_2 are shown in **Figure 5**. The curves are well described by exponentials $P \propto \exp(-\Gamma \tau_{NSE}/\hbar)$ (straight lines in the semilog
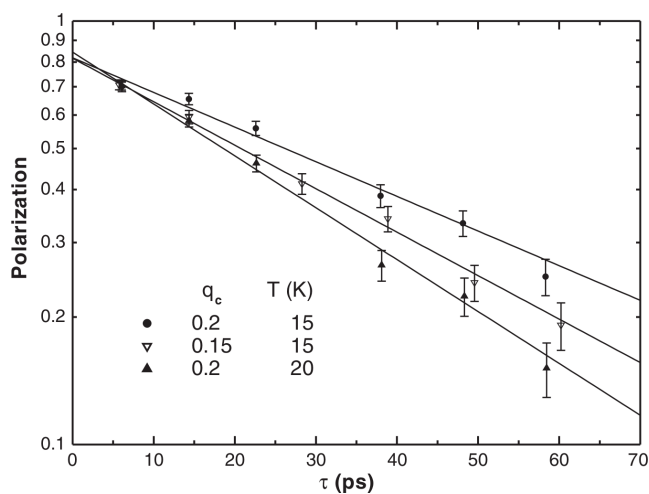

Figure 5. Raw spin-echo polarization data from MnF_2. Reproduced with permission.[30] Copyright 2006, AAAS.

plot), corresponding to Lorentzian $S(\omega)$. The difference in Γ between the central and the lower and upper curve is as small as $\pm 3\,\mu eV$, reflecting the good energy resolution of the NRSE technique. These raw data are then corrected for the resolution $F(\tau_{NSE})$ according to Equation 6 using the formalism of the study by Habicht et al.[53] including the slope and curvature of the dispersion. The latter were obtained from experimental magnon spectra, which look similar for both compounds, with a gap of $\approx 1\,meV$, zone boundary energies of $\approx 6\,meV$, and a softening of $\approx 10\%$ for $T = 0.5\,T_N$ compared with $T = 3K$.

The results are shown in **Figure 6**. The solid lines are a sum of two components, the linewidth calculated numerically using using four-magnon scattering and experimental dispersion curves and an additional residual linewidth at the lowest temperature (3 K) not reproduced by this calculation. The overall agreement of the calculation and the data are very good. At high T, the calculations underestimate the data, probably because higher-order magnon-scattering processes become significant. The residual linewidth at 3K is shown on an enlarged scale in Figure 6c. This contribution was identified to result from scattering of the magnons at domain walls, with the associated lifetime $\tau_D = d/[2v(q)]$, where d is the mean domain size and $v(q)$ is the magnon velocity given by the slope of the dispersion curve. The domain size $d \sim 0.5\,\mu m$ was determined by LD. The additional linewidth $\Gamma_D = h\tau_D^{-1}$ calculated with this simple model gives a satisfactory description of the 3K data.

The critical dynamics for $T \geq T_N$ were examined for both compounds by NRSE.[77] Here we focus on MnF_2. The high-resolution data allowed us to resolve contradicting results from previous TAS spectroscopy originating from insufficient energy resolution and to separate linewidths of longitudinal and transverse fluctuations. For the NRSE experiment, the crystal was aligned in the (H0L) plane, such that the longitudinal and transverse critical fluctuations corresponded to M_y and M_z in Figure 4, respectively. "Longitudinal" refers to the direction of the uniaxial spin ordering for $T < T_N$, namely, the crystallographic c-axis. The spin-echo polarization $P(\tau_{NSE})$ in **Figure 7**a−c shows fast oscillations for small τ_{NSE}, resulting from the interference of spin-flip scattering from M_y and M_z. The linewidths $\Gamma_\parallel$ and $\Gamma_\perp$ in (d,e) were extracted by a numerical simulation of the Larmor precession and spin-flip processes, as the simple analysis by Equation (1) and (3) fails for the oscillating P. $\Gamma_\parallel$ shows critical slowing down and a crossover from 3D Heisenberg to 3D Ising scaling, whereas $\Gamma_\perp$ shows no critical behavior. The intensity ratio $I_\perp/I_\parallel$ is dominated by the longitudinal fluctuations close to T_N and approaches unity for $T \gg T_N$.

5.2. Spin Excitations in a 1D Quantum Magnet

In the standard picture, a spin excitation decays exponentially in the time domain by collisions with other excitations. This exponential decay leads to a Lorentzian lineshape $S(\omega)$ in energy. With increasing temperature, the collisions become more frequent, and the width Γ of the Lorentzian increases. This simple picture fails in 1D systems with hard-core interactions, where strong deviations from the exponential decay and thus non-Lorentzian asymmetric lineshapes in energy are expected.[78] A model system for such a 1D spin-1/2 antiferromagnet is
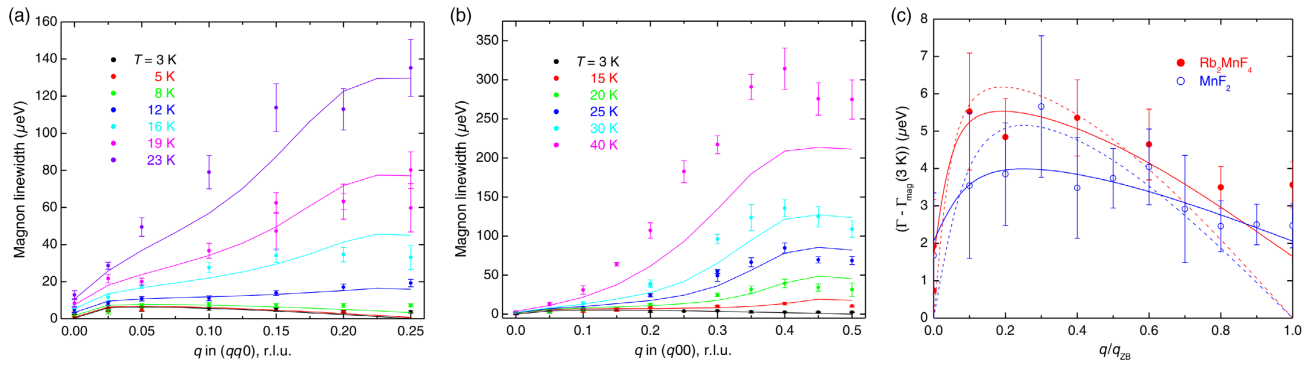
Figure 6. Magnon linewidth data over the BZ for a) Rb_2MnF_4 and b) MnF_2. The curves show calculations based on four-magnon scattering. c) Linewidth data at 3K for Rb_2MnF_4 (red) and MnF_2 (blue). The dashed lines were calculated for ballistic magnon propagation between the domain walls. The solid lines contain an additional linear contribution. Reproduced with permission.[75] Copyright 2013, APS.
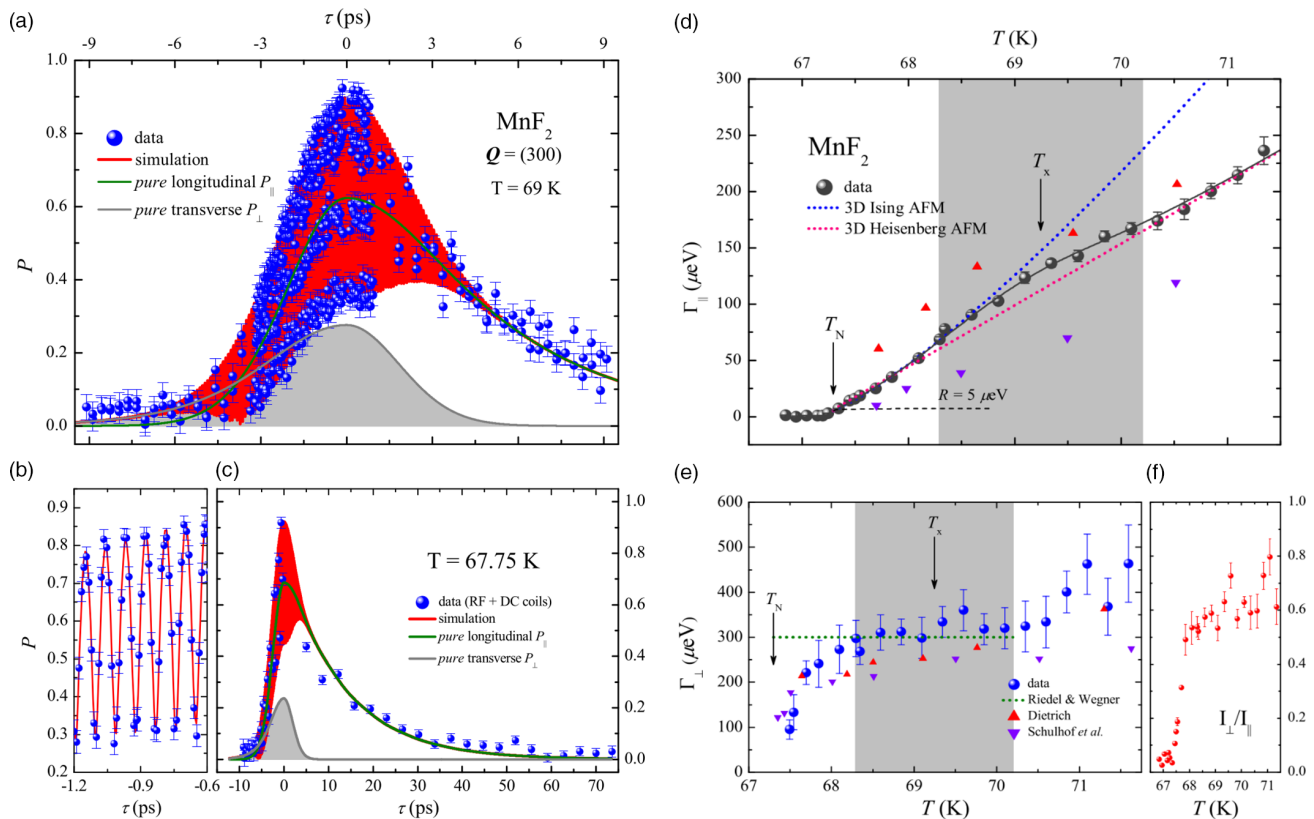

Figure 7. Spin-echo polarization data on critical dynamics in MnF_2 ($T_N = 67.3K$). a) $T = 69K$. c) $T = 67.75K$. b) Zoom to fast oscillation of the polarization in (a). Temperature dependence of $\Gamma_\parallel$ d) and $\Gamma_\perp$. e,f) Ratio of integrated intensities $I_\perp / I_\parallel$. Reproduced with permission.[77] Copyright 2016, APS.

copper nitrate $[Cu(NO)_2 \cdot 2.5D_2O]$. TOF neutron spectroscopy found the expected asymmetric $S(\omega)$, but in view of the elaborate data analysis including deconvolution with the TOF instrumental resolution on a strongly sloping signal background, a confirmation of the results by the independent NRSE was suggested.[79] NRSE offers two advantages for this study, including the direct observation of the decay in the time domain, and the insensitivity to the sloping background, which only gives a constant factor reducing $P(\tau_{NSE})$. In contrast to the majority of N(R)SE experiments, where only the magnitude of P is analyzed, here also the

phase of P (**Figure 8**b) was included in the data analysis, as the latter also carries information about the excitation energy and lineshape.[80,81] The resulting $S(\omega)$ in Figure 8a shows a clear evolution of the asymmetric broadening with temperature and thus confirms previous TOF data.

5.3. Magnetic Ordering and Structural Effects

Ordering phenomena of the electron system usually cause a response of the crystal lattice or are vice versa triggered by a
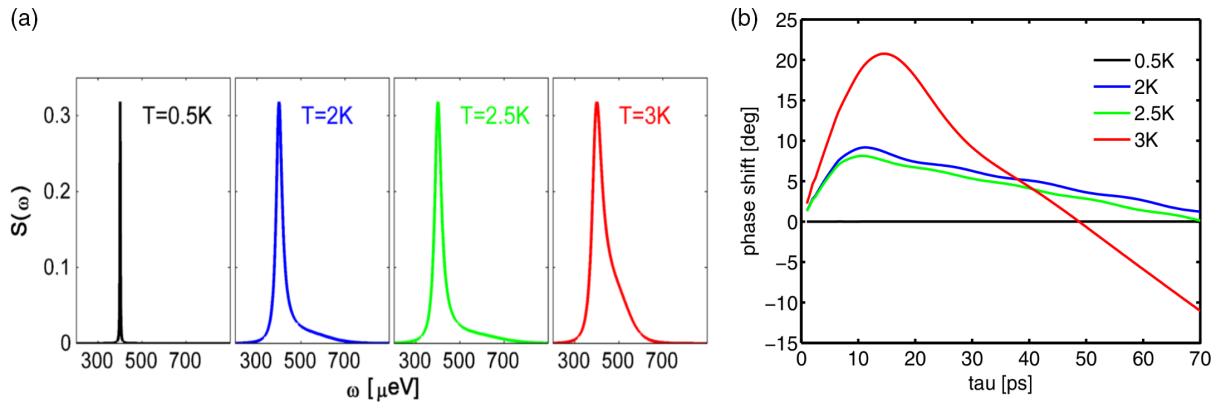
(a)

(b)

Figure 8. a) Linewidth of the one-magnon mode in copper nitrate at the minimum of the dispersion corresponding to $Q = (101)$. b) Phase of $P(\tau_{NSE})$. Reproduced with permission.[80] Copyright 2016, APS.

structural transition. The structural effects observable by LD include anomalies in the thermal expansion, structural transitions, small distortions of the structure, and, on a mesoscopic scale, the formation of structural and magnetic domains. Thermal expansion is usually measured by capacitive dilatometry with a resolution superior to LD. The latter is unique if conducting dilatometry is challenging, as in the case of high pressures and high temperatures. LD moreover is sensitive to specific crystallographic directions by selection of appropriate Bragg peaks, even in polycrystalline samples. Examples for LD experiments at high pressures include a study of the thermal expansion of MnSi[82] to elucidate the nature of a non-Fermi liquid state and a study related to the hidden-order phase in URu_2Si_2.[83] LD studies on iron pnictides, partially under uniaxial pressure, helped to elucidate the interplay between the orthorhombic-to-tetragonal phase transition, AFM ordering, and superconductivity.[84–86] A further example is the structural phase transition in an iron pnictide, where the expected orthorhombic splitting of a Bragg peak is not visible in conventional diffraction due to the large intrinsic width of the peaks, whereas it was unambiguously detected by LD.[87]

Finally, we discuss an example of mesoscopic structural domains in undoped, AFM $YBa_2Cu_3O_{6.0}$. The data in **Figure 9** show the polarization $P(\phi_{LD})$ for the (220) and (200) Bragg peaks above and below the Néel temperature $T_N = 420$K. The data $P(\phi_{LD})$ are well described by Equation 12, assuming Gaussian distributions D. The widths look quite different, but have the same ratio $\sqrt{2}$ as the corresponding reciprocal lattice vectors, and are thus consistent with square-shaped domains of characteristic width $L_\parallel = 370$ nm in the CuO_2 planes. The domain size in the perpendicular direction obtained from the (006) data is $L_\perp = 390$ nm. This structural domain formation probably results from impurities and associated microstrains. Below T_N the domain shape stays unchanged but shrinks by about 10% as a consequence of magnetostriction effects. The characteristic width of the AFM domains of 240 nm is smaller than those of the structural domains, consistent with the assumption that structural domain boundaries disrupt magnetic order.
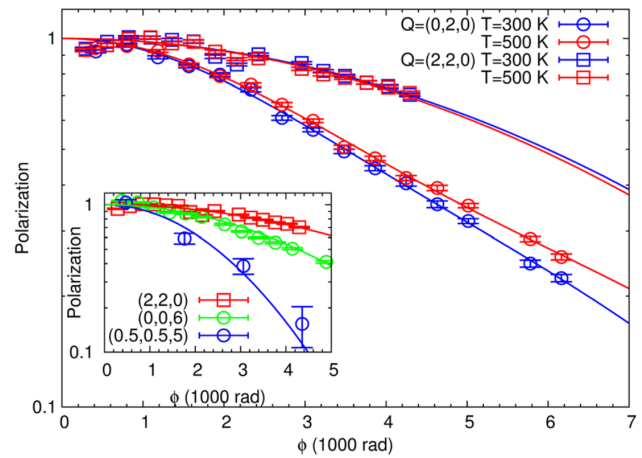

Figure 9. LD polarization data versus total Larmor phase for the (220) and (200) Bragg peaks in $YBa_2Cu_3O_{6.0}$, at temperatures below and above $T_N = 420$ K. Inset: (220), (006), and $(\frac{1}{2}\frac{1}{2}5)$ at $T = 40$ K. Reproduced with permission.[90] Copyright 2016, APS.

6. Conclusion

Neutron spin echo offers versatile instrumental configurations for the study of spin excitations and structural effects related to magnetic ordering. Experimentally challenging is the study of neutron spin-depolarizing ferromagnetic samples with domains or samples in high fields, both for spectroscopy and LD. There are two solutions for spectroscopy, but both are associated with severe limitations. The IMNSE configuration requires an additional PO/AN pair close to the sample, at the cost of an intensity loss of at least 75%. MIEZE, in contrast, needs no additional POs, and magnetic fields of 17Tesla were applied to the sample, but the resolution decreases with increasing momentum transfer due to an increasing variance of the path lengths of neutron trajectories across the sample. In addition, there is at present no solution allowing applications of MIEZE to dispersive excitations.

In the case of LD, the situation is more favorable. There are several solutions to cope with spin-depolarizing samples, all with their specific drawbacks. First, there is Rekveldt's single-arm LD (Figure 3b). It was originally designed for implementing LD at powder diffractometers with multiangle detectors, and it is insensitive to depolarizing samples. The main limitation is that the resolution (Figure 3a) is reduced by one order of magnitude compared with full LD and strongly depends on the scattering angle and beam collimation. These disadvantages are partially compensated by combining MIEZE with LD ((Figure 3c),[88,89]). The resolution of this setup approaches the one of full LD for small samples of dimension ≈ 1 mm but also depends on path length variance in the sample.

Currently, the first dedicated Larmor diffractometer LADIFF is under construction at the MLZ, using the main components of the TAS FLEXX from HZB. LADIFF is based on transverse RF flippers and will offer the aforementioned options for depolarizing samples in strong magnetic fields.

Conflict of Interest

The authors declare no conflict of interest.

[1] F. Mezei, *Z. Phys. A* **1972**, *255*, 146.
[2] *Neutron Spin Echo* (Ed: F. Mezei), Lecture Notes in Physics, Vol. 128, Springer, Berlin **1980**.
[3] F. Mezei, A. Murani, *J. Magn. Magn. Mater.* **1979**, *14*, 211.
[4] F. Mezei, *Phys. Rev. Lett.* **1982**, *49*, 1096.
[5] B. Farago, F. Mezei, *Physica B+C* **1986**, *136*, 100.
[6] F. Mezei, G. Drabkin, A. Ioffe, *Physica B* **2001**, *297*, 9.
[7] *Neutron Spin Echo Spectroscopy* (Eds: F. Mezei, T. Gutberlet, C. Pappas), Lecture Notes in Physics, Vol. 601, Springer, Berlin **2003**.
[8] P. Schleger, G. Ehlers, A. Kollmar, B. Alefeld, J. Barthelemy, H. Casalta, B. Farago, P. Giraud, C. Hayes, C. Lartigue, F. Mezei, D. Richter, *Physica B: Condens. Matter* **1999**, *266*, 49.
[9] B. Farago, P. Falus, I. Hoffmann, M. Gradzielski, F. Thomas, C. Gomez, *Neutron News* **2015**, *26*, 15.
[10] N. Rosov, S. Rathgeber, M. Monkenbusch, in *Scattering From Polymers*, ACS Symposium Series, Vol. *739*, American Chemical Society, Washington, DC **2000**, pp. 103–116.
[11] M. Ohl, M. Monkenbusch, N. Arend, T. Kozielewski, G. Vehres, C. Tiemann, M. Butzek, H. Soltner, U. Giesen, R. Achten, H. Stelzer, B. Lindenau, A. Budwig, H. Kleines, M. Drochner,

[12] S. Pasini, O. Holderer, T. Kozielewski, D. Richter, M. Monkenbusch, *Rev. Sci. Instrum.* **2019**, *90*, 043107.
[13] G. Ehlers, *J. Phys.: Condens. Matter* **2006**, *18*, R231.
[14] B. Farago, *Physica B* **1997**, *241–243*, 113.
[15] C. Pappas, G. Kali, T. Krist, P. Böni, F. Mezei, *Phys. B* **2000**, *283*, 365.
[16] C. Pappas, E. Leliévre-Berna, P. Bentley, E. Bourgeat-Lami, E. Moskvin, M. Thomas, S. Grigoriev, V. Dyadkin, *Nucl. Instrum. Methods A* **2008**, *592*, 420.
[17] E. Leliévre-Berna, P. Bentley, E. Bourgeat-Lami, M. Thomas, C. Pappas, R. Kischnik, E. Moskvin, *Physica B* **2009**, *404*, 2624.
[18] R. M. Moon, T. Riste, W. C. Koehler, *Phys. Rev.* **1969**, *181*, 920.
[19] C. Pappas, E. Lelièvre-Berna, P. Bentley, P. Falus, P. Fouquet, B. Farago, *Phys. Rev. B* **2011**, *83*, 224405.
[20] L. J. Bannenberg, K. Kakurai, P. Falus, E. Lelièvre-Berna, R. Dalgliesh, C. D. Dewhurst, F. Qian, Y. Onose, Y. Endoh, Y. Tokura, C. Pappas, *Phys. Rev. B* **2017**, *95*, 144433.
[21] P. Fouquet, G. Ehlers, B. Farago, C. Pappas, F. Mezei, *J. Neutron Res.* **2007**, *15*, 39.
[22] R. Gähler, R. Golub, *J. Phys. (France)* **1988**, *49*, 1195.
[23] R. Golub, R. Gähler, *Phys. Lett. A* **1987**, *123*, 43.
[24] F. Mezei, in *Neutron Inelastic Scattering*, IAEA, Vienna **1978**, p. 125.
[25] M. T. Rekveldt, T. Keller, R. Golub, *Europhys. Lett.* **2001**, *54*, 342.
[26] T. Keller, R. Golub, F. Mezei, R. Gahler, *Physica B* **1997**, *241–243*, 101.
[27] F. Groitl, T. Keller, D. L. Quintero-Castro, K. Habicht, *Rev. Sci. Instrum.* **2015**, *86*, 025110.
[28] T. Keller, K. Habicht, H. Klann, M. Ohl, H. Schneider, B. Keimer, *Appl. Phys. A* **2002**, *74*, s332.
[29] N. Martin, L.-P. Regnault, S. Klimko, J. Lorenzo, R. Gähler, *Physica B* **2011**, *406*, 2333.
[30] S. Bayrakci, T. Keller, K. Habicht, B. Keimer, *Science* **2006**, *312*, 1926.
[31] B. Náfrádi, T. Keller, H. Manaka, A. Zheludev, B. Keimer, *Phys. Rev. Lett.* **2011**, *106*, 177202.
[32] A. L. Chernyshev, M. E. Zhitomirsky, N. Martin, L.-P. Regnault, *Phys. Rev. Lett.* **2012**, *109*, 097201.
[33] C. Zeyen, *J. Phys. Chem. Solids* **1999**, *60*, 1573.
[34] C. M. E. Zeyen, P. C. Rem, *Meas. Sci. Technol.* **1996**, *7*, 782.
[35] M. Nishi, K. Kakurai, *Physica B* **2002**, *311*, 70.
[36] J. Kulda, A. Debernardi, M. Cardona, F. de Geuser, E. E. Haller, *Phys. Rev. B* **2004**, *69*, 045209.
[37] F. Li, S. R. Parnell, T. Wang, D. V. Baxter, R. Pynn, *J. Phys. Conf. Ser.* **2016**, *711* 012015.
[38] F. Li, R. Pynn, *J. Appl. Crystallogr.* **2014**, *47*, 1849.
[39] F. Li, J. Shen, S. R. Parnell, A. N. Thaler, M. Matsuda, T. Keller, O. Delaire, R. Pynn, J. A. Fernandez-Baca, *J. Appl. Crystallogr.* **2019**, *52*, 755.
[40] F. Li, H. Feng, A. N. Thaler, S. R. Parnell, W. A. Hamilton, L. Crow, W. Yang, A. B. Jones, H. Bai, M. Matsuda, D. V. Baxter, T. Keller, J. A. Fernandez-Baca, R. Pynn, *Sci. Rep.* **2017**, *7*, 865.
[41] R. Gahler, R. Golub, T. Keller, *Physica B* **1992**, *180–181*, 899.
[42] M. Krautloher, J. Kindervater, T. Keller, W. Häussler, *Rev. Sci. Instrum.* **2016**, *87*, 125110.
[43] H. Endo, T. Oda, M. Hino, T. Hosobata, *Physica B* **2019**, *564*, 91.
[44] R. Dalgliesh, S. Langridge, J. Plomp, V. de Haan, A. van Well, *Physica B* **2011**, *406*, 2346.
[45] J. Plomp, V. de Haan, R. Dalgliesh, S. Langridge, A. van Well, *Thin Solid Films* **2007**, *515*, 5732.
[46] N. Geerits, S. R. Parnell, M. A. Thijs, A. A. van Well, C. Franz, A. L. Washington, D. Raspino, R. M. Dalgliesh, J. Plomp, *Rev. Sci. Instrum.* **2019**, *90*, 125101.
[47] T. Keller, R. Gahler, H. Kunze, R. Golub, *Neutron News* **1995**, *6*, 16.
[48] M. Rekveldt, *Nucl. Instrum. Methods B* **1996**, *114*, 366.

[49] M. Strobl, M. Sales, J. Plomp, W. G. Bouwman, A. S. Tremsin, A. Kaestner, C. Pappas, K. Habicht, *Sci. Rep.* **2015**, *5*, 16576.
[50] M. Sales, J. Plomp, K. Habicht, A. Tremsin, W. Bouwman, M. Strobl, *Rev. Sci. Instrum.* **2016**, *87*, 063907.
[51] R. Gähler, R. Golub, K. Habicht, T. Keller, J. Felber, *Physica B* **1996**, *229*, 1.
[52] J. Felber, R. Gähler, R. Golub, K. Prechtel, *Physica B* **1998**, *252*, 1 34.
[53] K. Habicht, T. Keller, R. Golub, *J. Appl. Crystallogr.* **2003**, *36*, 1307.
[54] F. Groitl, T. Keller, K. Habicht, *J. Appl. Crystallogr.* **2018**, *51*, 818.
[55] C. Franz, S. Säubert, A. Wendl, F. X. Haslbeck, O. Soltwedel, J. K. Jochum, L. Spitz, J. Kindervater, A. Bauer, P. Böni, C. Pfleiderer, *J. Phys. Soc. Jpn.* **2019**, *88*, 081002.
[56] T. Rekveldt, W. Kraan, *Nucl. Instrum. Methods A* **2011**, *629*, 239.
[57] J. Major, H. Dosch, G. Felcher, K. Habicht, T. Keller, S. te Velthuis, A. Vorobiev, M. Wahl, *Physica B* **2003**, *336*, 8.
[58] G. P. Felcher, S. G. E. te Velthuis, J. Major, H. Dosch, C. Anderson, K. Habicht, T. Keller, in *Advances in Neutron Scattering Instrumentation*, Proc. SPIE Vol. *4785* (Eds: I. S. Anderson, B. Guérard), International Society for Optics and Photonics, SPIE, Washington, DC **2002** pp. 164–173.
[59] J. Major, A. Vorobiev, A. Rühm, R. Maier, M. Major, M. Mezger, M. Nülle, H. Dosch, G. P. Felcher, P. Falus, T. Keller, R. Pynn, *Rev. Sci. Instrum.* **2009**, *80*, 123903.
[60] M. T. Rekveldt, W. G. Bouwman, W. H. Kraan, O. Uca, S. V. Grigoriev, K. Habicht, T. Keller, in *Elastic Neutron Scattering Measurements Using Larmor Precession of Polarized Neutrons*, Springer Berlin Heidelberg, Berlin, Heidelberg **2003**, pp. 87–99.
[61] W. G. Bouwman, J. Plomp, V. O. de Haan, W. H. Kraan, A. A. van Well, K. Habicht, T. Keller, M. T. Rekveldt, *Nucl. Instrum. Methods A* **2008**, *586*, 9.
[62] F. Li, R. Dadisman, D. C. Wasilko, *Nucl. Instrum. Methods A* **2020**, *955*, 163300.
[63] R. Gähler, R. Golub, *Z. Phys. B* **1984**, *56*, 5.
[64] J. K. Jochum, A. Wendl, T. Keller, C. Franz, *Meas. Sci. Technol.* **2019**, *31*, 035902.
[65] S. Säubert, J. Kindervater, F. Haslbeck, C. Franz, M. Skoulatos, P. Böni, *Phys. Rev. B* **2019**, *99*, 184423.
[66] F. Haslbeck, S. Säubert, M. Seifert, C. Franz, M. Schulz, A. Heinemann, T. Keller, P. Das, J. D. Thompson, E. D. Bauer, C. Pfleiderer, M. Janoschek, *Phys. Rev. B* **2019**, *99*, 014429.
[67] J. Kindervater, N. Martin, W. Häußler, M. Krautloher, C. Fuchs, S. Mühlbauer, J. A. Lim, E. Blackburn, P. Böni, C. Pfleiderer, *EPJ Web Conf.* **2015**, *83* 03008.
[68] G. Brandl, R. Georgii, W. Häußler, S. Mühlbauer, P. Böni, *Nucl. Instrum. Methods A* **2011**, *654*, 394.
[69] T. Weber, G. Brandl, R. Georgii, W. Häubler, S. Weichselbaumer, P. Böni, *Nucl. Instrum. Methods A* **2013**, *713*, 71.
[70] M. T. Rekveldt, *Physica B* **2000**, *276–278*, 55.
[71] T. Keller, P. Fabrykiewicz, R. Przeniosło, I. Sosnowska, B. Keimer, *J. Appl. Crystallogr.* **2020**, *53*, 88.
[72] M. T. Rekveldt, J. Plomp, A. A. van Well, *J. Appl. Crystallogr.* **2014**, *47*, 436.
[73] A. van Well, M. Rekveldt, *J. Phys. Conf. Ser.* **2017**, *862* 012029.
[74] M. T. Rekveldt, *Z. Phys.* **1973**, *259*, 391.
[75] S. P. Bayrakci, D. A. Tennant, P. Leininger, T. Keller, M. C. R. Gibson, S. D. Wilson, R. J. Birgeneau, B. Keimer, *Phys. Rev. Lett.* **2013**, *111*, 017204.
[76] S. P. Bayrakci, B. Keimer, D. A. Tennant, arxiv1302.6476, **2013**.
[77] K. F. Tseng, T. Keller, A. C. Walters, R. J. Birgeneau, B. Keimer, *Phys. Rev. B* **2016**, *94*, 014424.
[78] B. Fauseweh, F. Groitl, T. Keller, K. Rolfs, D. A. Tennant, K. Habicht, G. S. Uhrig, *Phys. Rev. B* **2016**, *94*, 180404.
[79] D. A. Tennant, B. Lake, A. J. A. James, F. H. L. Essler, S. Notbohm, H.-J. Mikeska, J. Fielden, P. Kögerler, P. C. Canfield, M. T. F. Telling, *Phys. Rev. B* **2012**, *85*, 014402.
[80] F. Groitl, T. Keller, K. Rolfs, D. A. Tennant, K. Habicht, *Phys. Rev. B* **2016**, *93*, 134404.
[81] F. Groitl, *Ph.D. Thesis*, TU Berlin, **2012**.
[82] C. Pfleiderer, P. Böni, T. Keller, U. K. Rößler, A. Rosch, *Science* **2007**, *316*, 1871.
[83] P. G. Niklowitz, C. Pfleiderer, T. Keller, M. Vojta, Y.-K. Huang, J. A. Mydosh, *Phys. Rev. Lett.* **2010**, *104*, 106406.
[84] X. Lu, D. W. Tam, C. Zhang, H. Luo, M. Wang, R. Zhang, L. W. Harriger, T. Keller, B. Keimer, L.-P. Regnault, T. A. Maier, P. Dai, *Phys. Rev. B* **2014**, *90*, 024509.
[85] X. Lu, K.-F. Tseng, T. Keller, W. Zhang, D. Hu, Y. Song, H. Man, J. T. Park, H. Luo, S. Li, A. H. Nevidomskyy, P. Dai, *Phys. Rev. B* **2016**, *93*, 134519.
[86] W. Wang, Y. Song, C. Cao, K.-F. Tseng, T. Keller, Y. Li, L. W. Harriger, W. Tian, S. Chi, R. Yu, A. H. Nevidomskyy, P. Dai, *Nat. Commun.* **2018**, *9*, 3128.
[87] D. S. Inosov, G. Friemel, J. T. Park, A. C. Walters, Y. Texier, Y. Laplace, J. Bobroff, V. Hinkov, D. L. Sun, Y. Liu, R. Khasanov, K. Sedlak, P. Bourges, Y. Sidis, A. Ivanov, C. T. Lin, T. Keller, B. Keimer, *Phys. Rev. B* **2013**, *87*, 224425.
[88] K. Habicht, Habilitationsschrift, Universität Potsdam, **2016**.
[89] K. Habicht, T. Keller, *Neutron Larmor Diffraction on Ferromagnetic Samples*, Unpublished.
[90] B. Náfrádi, T. Keller, F. Hardy, C. Meingast, A. Erb, B. Keimer, *Phys. Rev. Lett.* **2016**, *116*, 047001.